SUMMARY OF THE R&D PERFORMED AT IPN ORSAY FOR THE ALICE DIMUON TRACKING CHAMBERS

N. Willis, Y. Le Bornec, L. Bimbot,
P. Courtat, C. Diarra, R. Kunne,
M. Mac Cormick and J.M. Martin
Institut de Physique Nucléaire, IN2P3/Université Paris-Sud, B.P. N⁰ 1,
F-91406, Orsay, FRANCE

P. Bhattacharya, S. Bose, S. Chattopadhyay and P. Sen
Saha Institute of Nuclear Physics, 1/AF, Bidhan Nagar, Kolkata - 700 064,
INDIA

Abstract

The dimuon arm of the LHC detector ALICE, will be equipped with pad and cathode strip chambers. An R&D program has been launched at IPN to optimize the characteristics of these chambers, both the front-end and the read-out electronics. The present report gives the description of the tests carried out at CERN-SPS. The test beam data has been analyzed and a comparison between the experimental results and the simulation calculations has been presented.

Chapter 1

Introduction

The tracking system of the ALICE dimuon arm is composed of five stations with two chambers each. In order to fulfill both the requirements of spatial resolution and of high counting rate capability, pad chambers have been chosen. For instance, the first two chambers, which are located just behind the 5 meters long front absorber, will detect several hundreds of particles emitted in one single central Pb-Pb collision.

In order to optimize the internal geometry of the station 1 chambers and to find a compromise between their performance and the number of electronic channels, a R&D program has been undertaken. In a first step the different geometrical parameters such as the ratio of pad widths over anode-cathode distance or the anode pitch have been defined. Recently the particle background was estimated more precisely through simulation using the code FLUKA. This have imposed more stringent requirements on granularity of the cathode pads. A new pad size of 4x6 mm^2 has been adapted for the inner region of Station 1, close to the beam pipe, which has been validated after the in-beam tests described below.

This report has several goals:

- to present the obtained experimental results and the performance of the detector

- to present the simulation results compared to the experimental ones

- to provide the inputs of the simulation calculations useful for their use in the most general frame of the dimuon arm and more generally of ALICE.

Chapter 2

EXPERIMENTAL SET-UP

2.1 SPS Beam

The in-beam tests have been performed in May-June 2000 at the SPS beam line H4 with 350 Gev/c π^- incident particles. The spill duration was about 2.5 sec every 20 sec. The typical intensity was approximately 1000 particles/spill and the size of the beam spot on the studied prototype was about 2x2 cm^2 in accordance with the size of the tracker described below.

2.2 Silicon tracker and trigger system

The reference tracks were reconstructed using a telescope composed of 10 planes of silicon strip detectors. Each of these detectors was composed of 196 adjacent strips which are 50 μm wide and 2 cm long. Their spatial resolutions were estimated to be around 12 μm. Multiple scattering effects in the different material layers were found to be negligible at this high incident energy. The detectors were grouped in 5 pairs to provide the particle's coordinates (X and Y), perpendicular to the beam axis. Six planes of the tracker (3 X and 3 Y planes) were located upstream the pad chamber prototype and four were located downstream. This tracker system gave also the beam profile on the pad detector which is an essential input for the simulation calculations in order to reproduce the charge spectrum of each pad.

The trigger was generated through a coincidence between two pairs of crossed scintillators (2x2 cm^2) one of which is located before the first silicon plane while the other was placed ten meters behind the last plane.

2.3 The cathode pad Chamber

2.3.1 The detector

The general features of the prototype detectors have already been described [1]. Let's just recall that the two 40x40 cm^2 cathode surfaces were divided in four zones equipped with different pad sizes. The present manuscript reports the results obtained on one zone of 16x16 pads (4x6 mm^2 each), where the pads of one cathode were shifted by one half pad width in both the bending (X) and

Channel number	16
Noise at 0 pF	650 e$^-$rms
Noise slope	15 e$^-$/pF
Range	0 to 2 V
Linear dynamic range	-75 to 150 fC
Sensitivity- gain	11.2 mV/fC
Peaking time	from 450 up to 650 ns
Multiplexing frequency	maximum 10 MHz
Power consumption	8mW/channel

Table 2.1: GASSIPLEX 1.5 μm salient characteristics.

non-bending (Y) directions with respect to that for the other cathode. This geometry corresponds to the final configuration for the central part of the first station.

A binary gas mixture with 80% Ar and 20% CO_2 was used during these tests.

2.3.2 The front-end electronics

All the measurements presented below have been performed with a multiplexed system composed of pre-amplifiers read by means of a sequencer. The informations were digitized by a 10 bits ADC.

GASSIPLEX:

The well-known pre-amplifier-filter-shaper GASSIPLEX [5]was used. This version of the chip was made with 1.5 μm technology and the main characteristics are given in table 2.1

Each electronics board was composed of 4 GASSIPLEX and was connected to the pads by flexable kapton PCBs. The different boards were daisy chained. During the tests only 16 GASSIPLEX were chained.

Read-out and digitization:

The charge stored in the GASSIPLEX capacitors were successively read by means of a sequencer (CAEN V-550 and V-551) and digitized by a 10 bits ADC (CRAMS) with a 1.5 V range. The zero suppressed data were collected after the pedestal subtraction.

Performances:

The pedestal and noise of every channels were measured at regular interval during the test period. During the data taking, the individual gains of the different channels have not been calibrated. In the figures 2.1, 2.2, 2.3 and 2.4 the mean values of the pedestal and the noise of each channel of the two cathode planes are presented together with their frequency plot. These plots correspond to the measurements performed at HV= 1450V.

Figure 2.4 shows a mean value of 1.02 channels for the noise. Taking into account the ADC range of 1.5 V on 10 bits , the GASSIPLEX gain of 11.2
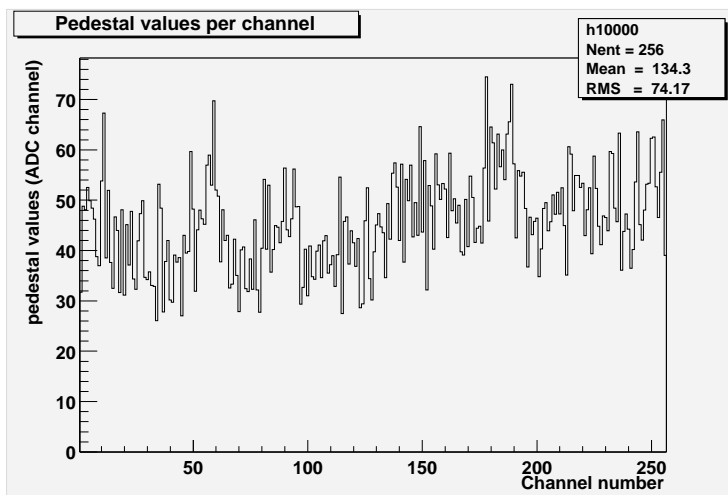
Figure 2.1: Pedestal for each channel of one cathode plane (in number of channels).
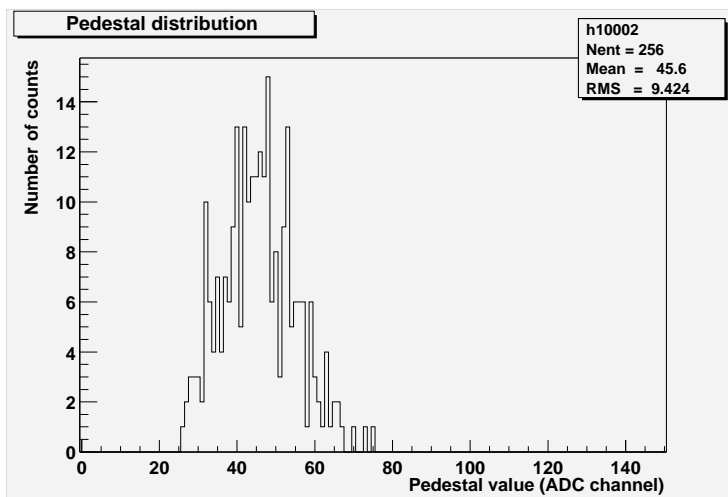

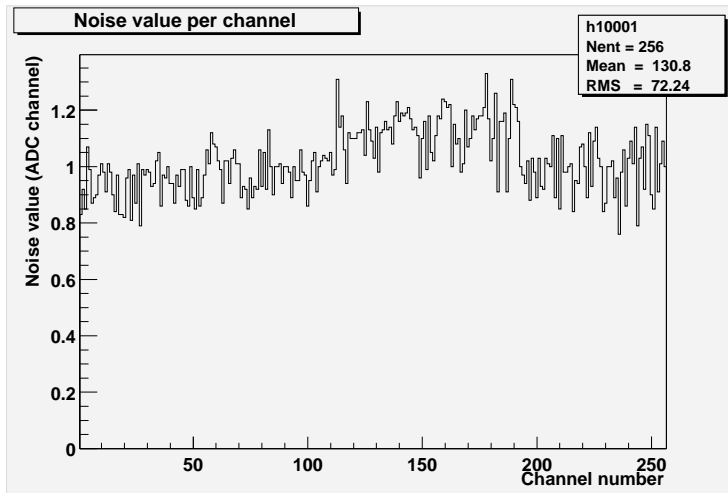Figure 2.2: Histogram of the pedestal values.

Figure 2.3: Noise for each channel of one cathode plane (in number of channels).
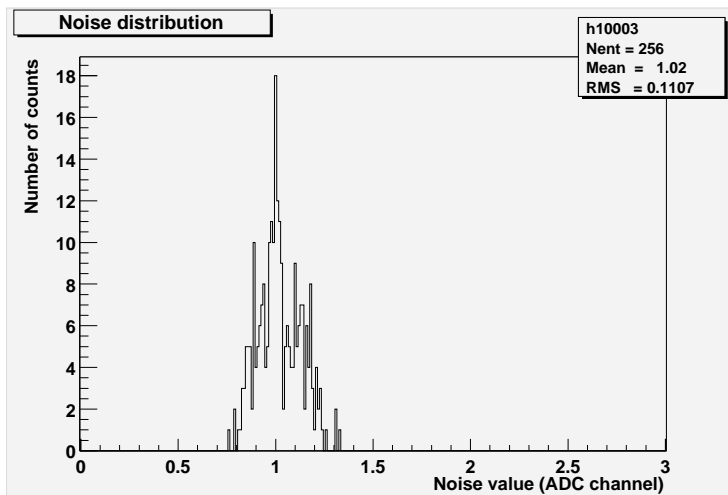

Figure 2.4: Histogram of the noise values.

mV/fC and the exit buffer gain equal to one, this mean noise corresponds to approximately 850 electrons.

D.A.Q.

The VME based acquisition system was base on DATE [2].

Chapter 3

EXPERIMENTAL AND SIMULATION RESULTS

3.1 Beam profiles

The tracks were reconstructed using the hit information from the silicon tracker following the standard procedure [3]. Each track was interpolated on the pad prototype and the experimental beam profile in the horizontal direction is shown in fig. 3.1 (upper part). A gaussian fit used for simulation purpose is presented in the lower part of the same figure. It is to be noted that the simulation does not take the inefficiency of the tracking system around 8.6 cm along the X-axis as shown in fig. 3.1.

3.2 Detector response

3.2.1 Total charge

Variation of the gain with the high voltage value.

The total charge induced by a minimum ionizing particle was measured by adding all the charges on each cathode plane. For measurements where the beam was normal to the chamber planes, the high voltage value was varied from 1375 V up to 1500 V by step of 25 V. Measurements at values higher than 1500 V have not been performed due to saturation in electronics.

Histograms of the total charge on both cathode planes are shown in figures 3.2 and 3.3 for different values of high voltage.

The saturation peaks are clearly visible in figures 3.2 and 3.3 with increasing high voltage values. The amplitude of the effect is different for the two cathode planes because the beam location relative to the pad positions is different on each cathode. This happens due to the small beam size and the staggering of the pads and thus the saturation occurs at lower HV on the plane 1 where the beam is centered on one pad.

The saturation effects start becoming important around 1450 V which is due to the high GASSIPLEX gain. The new version of the preamplifier which will be used in the final version of electronics has a 3 times lower gain.
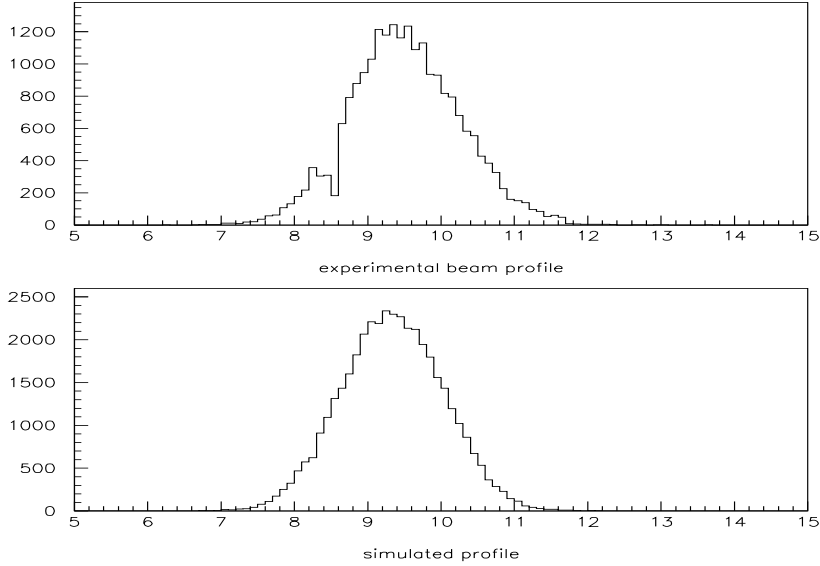
Figure 3.1: Measured and simulated beam-profiles at the level of the prototype in the horizontal plane.

HV value (V)	1375	1400	1425	1450	1475	1500
Landau MPV plane 1 (ADC channels)	145.7	200.3	275.9	372.3	520.5	747.9
Landau MPV plane2 (ADC channels)	135.5	186.3	260.7	348.4	484.9	678.3
plane 1 gain	$6.6\ 10^3$	$9.0\ 10^3$	$1.24\ 10^4$	$1.68\ 10^4$	$2.34\ 10^4$	$3.37\ 10^4$
plane 2 gain	$6.1\ 10^3$	$8.4\ 10^3$	$1.17\ 10^4$	$1.57\ 10^4$	$2.18\ 10^4$	$3.05\ 10^4$
2 plane gain differences	7.3%	7.2%	5.7%	6.6%	7.1%	9.8%

Table 3.1: Comparison of the two cathode plane gains versus HV values.

It is to be noted that the gain of the two cathode planes are not identical. A quantitative comparison of the gains for the two planes is shown in table 3.1 and fig.3.4 . With standard evaluation of primary ionisation (156 primary electrons/cm), it was estimated that about 62 primary electrons were produced in the gas volume of the prototype. With the hypothesis that, with a picking time of 600 ns, only one half of the total charge is collected and that the measured charge on a cathode is only one half of the total charge, we can evaluate the absolute gain of the detector which is given in table 3.1.

The gain increases by a factor 2 for a 53V variation in HV.

Cathode correlations

The correlation between the charges collected on the two planes, is particularly important for the suppression of fake tracks. The fig. 3.5 shows the satisfactory correlation.

The relative difference between the charges on the two planes is shown in
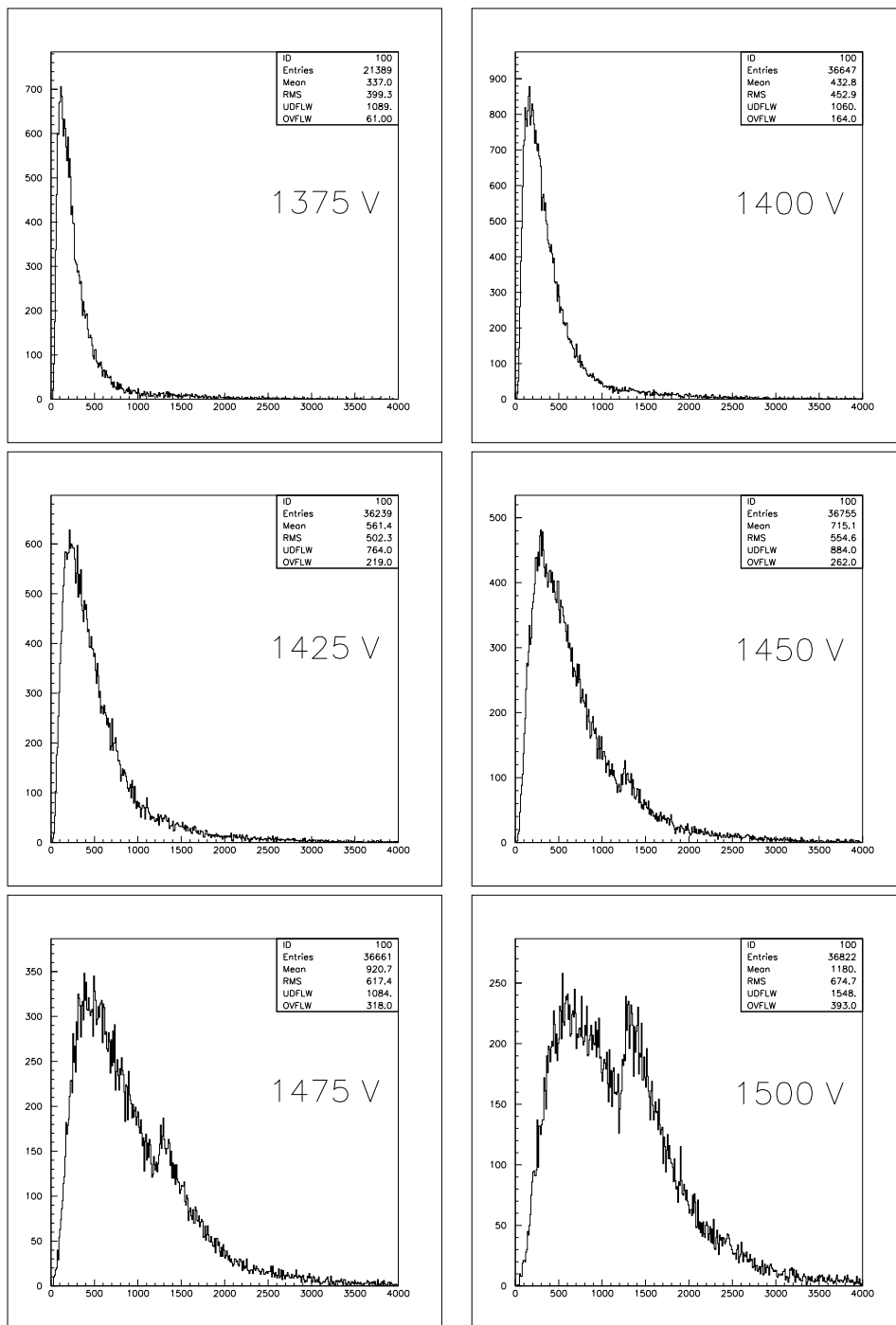
9

Figure 3.2: Variation of the signal for different HV values for the first cathode plane.
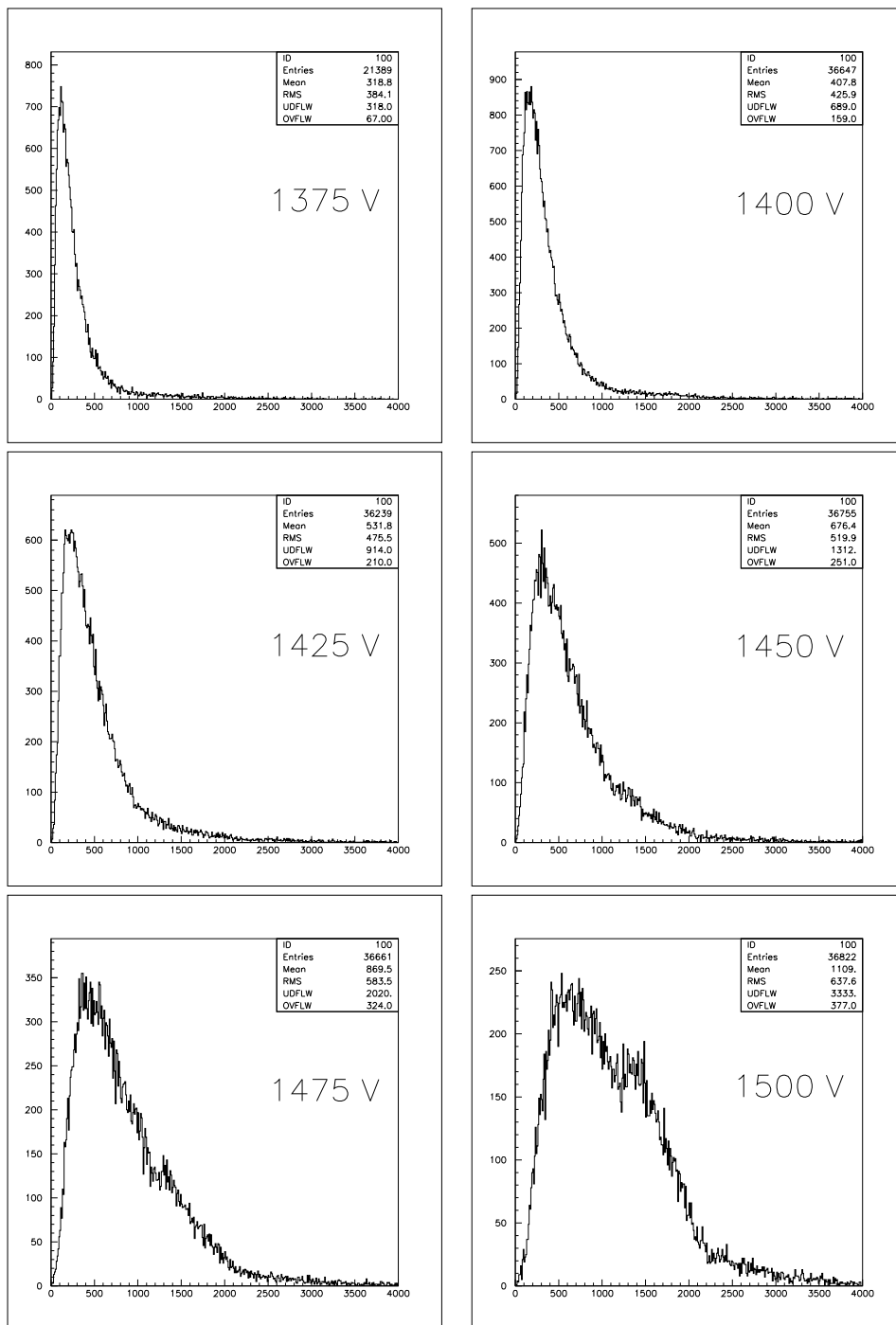
Figure 3.3: Variation of the signal for different HV values for the second cathode plane.
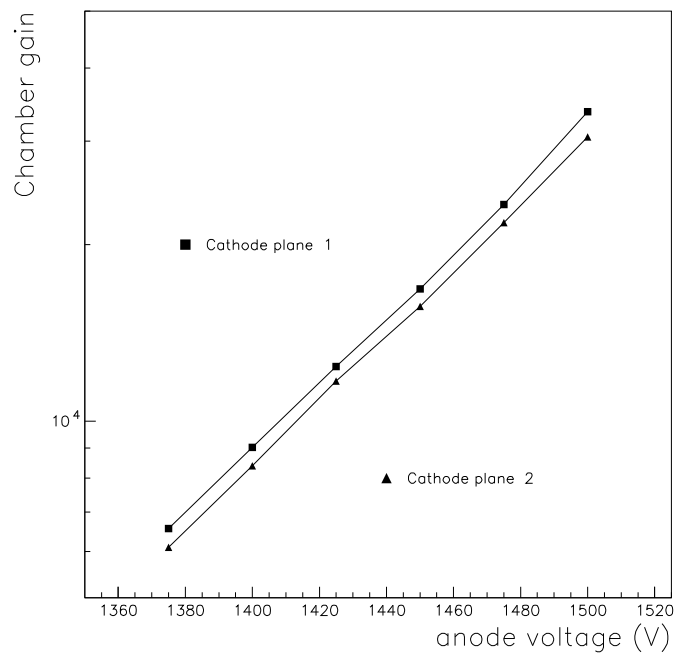
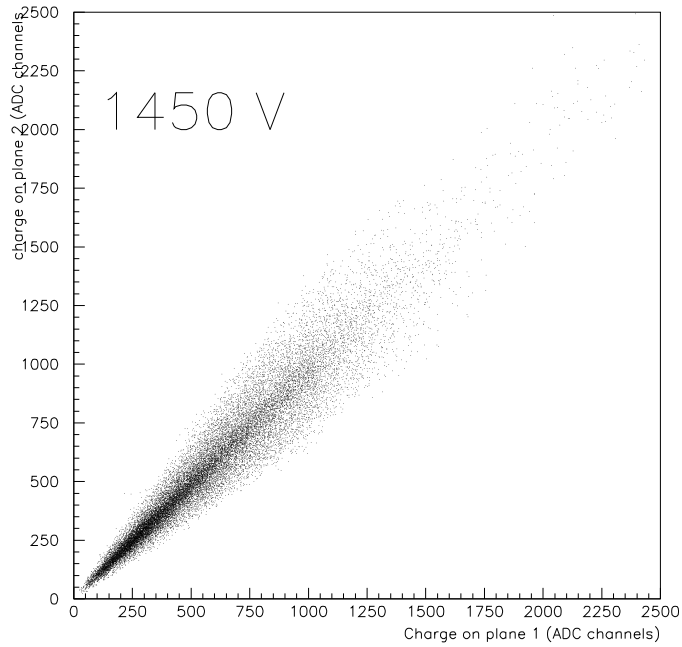Figure 3.4: Gains of the two cathode planes .vs. high voltage values.

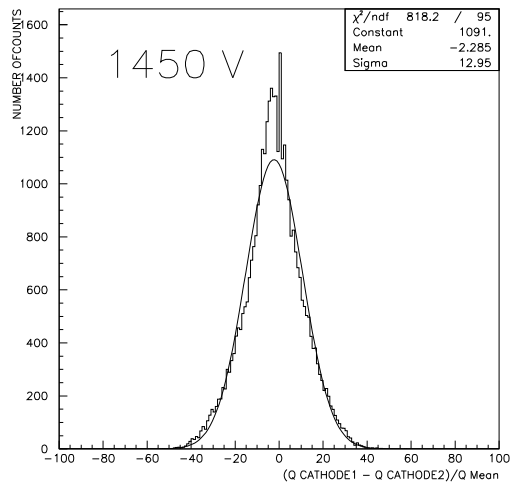Figure 3.5: Correlation between charges measured on the two cathode planes.

Figure 3.6: Difference of the charges measured on the two cathode planes normalized by the mean charge (in percentage).

fig. 3.6. The width of the distribution ($\sigma \sim 13\%$) does not depend significantly on the HV value.

3.2.2 Charge distribution

The knowledge of the shape of the charge distribution over the cathode plane is mandatory to calculate the position of the impact on the prototype using the measured charges on the pads. Thus it is necessary to reproduce these charges in the simulation code. The experimental maximum charge measured on the pads and normalized by the sum of the three neighbouring charges in X direction was calculated. Results are shown in fig. 3.7 as a function of the position of the hits calculated from the tracker information.

To reproduce this curve, the response function has to be integrated over the surface of the pads as a function of the location of the particle impact. Among several commonly used response functions, the Mathieson function has been found to be the most appropriate. From the literature [4], it is possible to extract the theoretical values of the relevant parameters $K_{3parall} = 0.558$ and $K_{3perp} = 0.683$ (parallel and perpendicular refering to the wire direction) as a function of geometrical characteristics: h/s (s is the anode pitch, h the anode-cathode distance) and on the ratio r_a/s (r_a is the anode wires radius).

A fit has been performed with h and K_3 as free parameters. Final values of $h = 1.75$ mm, $K_{3parall} = 0.52$ and $K_{3perp} = 0.57$ gave the best agreement with the experimental points as it can be seen on fig. 3.7.

Next step was to simulate total charge distribution as experimentally measured on each cathode (shown in figure 3.8 (right part)), where saturated events have been removed. A fit has been performed using a Landau function with two free parameters, the mean value and the width of the function. To extract the total charge distribution, the threshold was set to three times the noise variance on each pad (3σ) value as it has been done in the experimental analysis. The coding factor of 10 bits was also introduced and the beam profile function (shown in fig. 3.1) was used. A good agreement between simulation and data can be observed for non-saturated events and for all events (including saturations) on fig. 3.8 (left and right part respectively).

The histograms for individual pad charges are also presented in fig. 3.9 showing a good agreement between data and simulation.

An other way to check the validity of the simulations is to compare the calculated and measured ratio (R) of the charge on the central pad divided by the sum of the charges on the central and the two adjacent pads. The results are shown in fig. 3.10 which confirm the validity of the simulation.

The shift by half a pad between the two planes can be observed in fig. 3.11. It is to be noted that the two curves are not exactly in opposite phase but are slightly shifted by around 130 μm due to the relative shift between the two planes.

3.3 Analysis for different charge configurations

The large dynamic range of the chamber and the large gain of preamplifiers have led to various charge configurations which could be measured simultaneously in the bending direction of the detector. They were typically:
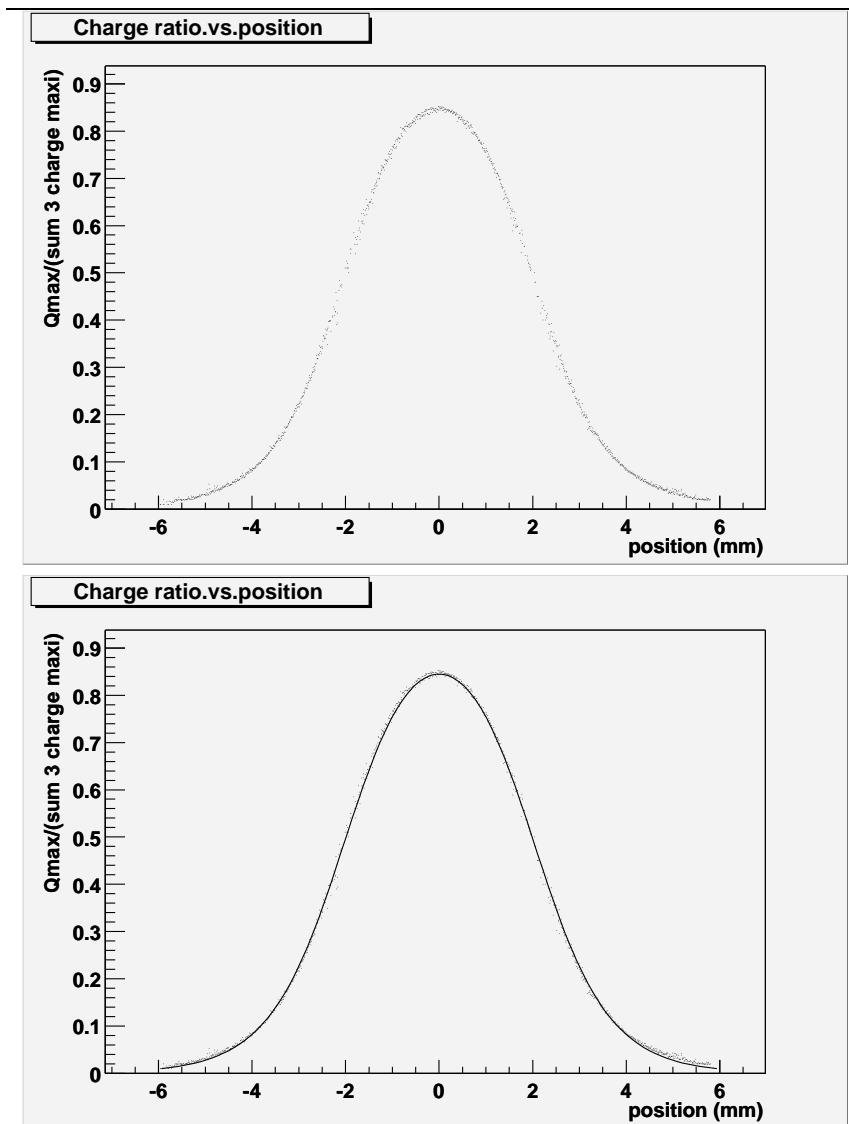
Figure 3.7: Value of the normalized charge measured on a pad versus the distance to the impact point (upper part).Comparison between the experimental integrated charge distribution and the theoretical curve obtained with a Mathieson function (lower part).
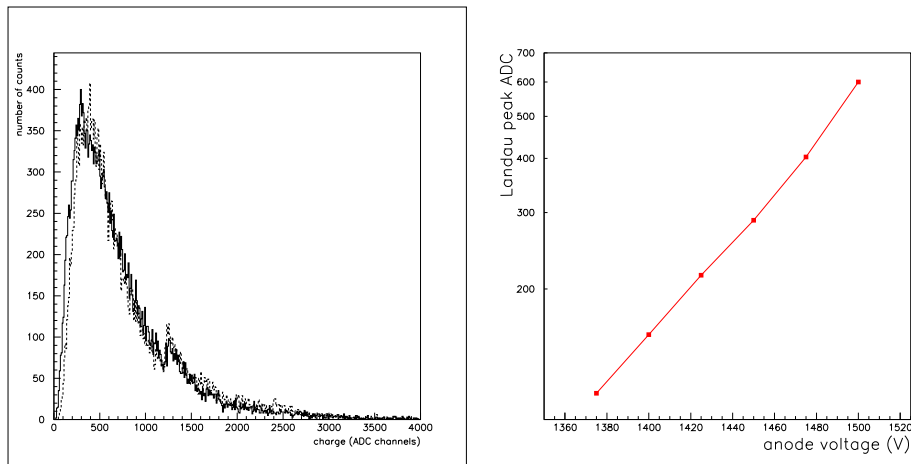
Figure 3.8: Experimental charge measured in the chamber (solid line) and the calculated charge (dashed line) for a 1450 V HV value with (left) and without (right) saturations.

1. 3 adjacent pads or more were hit without saturation

2. 3 adjacent pads or more were hit but the charges on the central pad was saturated

3. 3 adjacent pads or more are measured but the charges on two adjacent pads were saturated

4. only 2 adjacent pads were hit

5. only 1 pad was hit

6. unusable events (more than 100 hit pads, edge of the chamber...)

Hit pads are defined in a standard way as pads having a charge greater than a fixed threshold of three times the noise variance of each channel .

The relative importance of these different configurations depend on the HV value and on the location of the beam relative to the pads which depends in turn on the cathode plane. The percentage of the different configurations for both planes are tabulated in table 3.2 and are shown graphically in figures 3.12 and 3.13. Configurations 1, 2 and 4, which are the most important ones will be discussed in the next sections.

Nevertheless, it could be observed that configurations with two pads with saturated charges are not negligeable at the highest high voltage and even more for the cathod plane 2 (23.1% at 1500 V for example). This will not be the case with the electronics foreseen for the definitive detector.

An important quantity for the occupation factor is the number of pads hit per event. The measured values versus the HV values are plotted in fig. 3.14 .
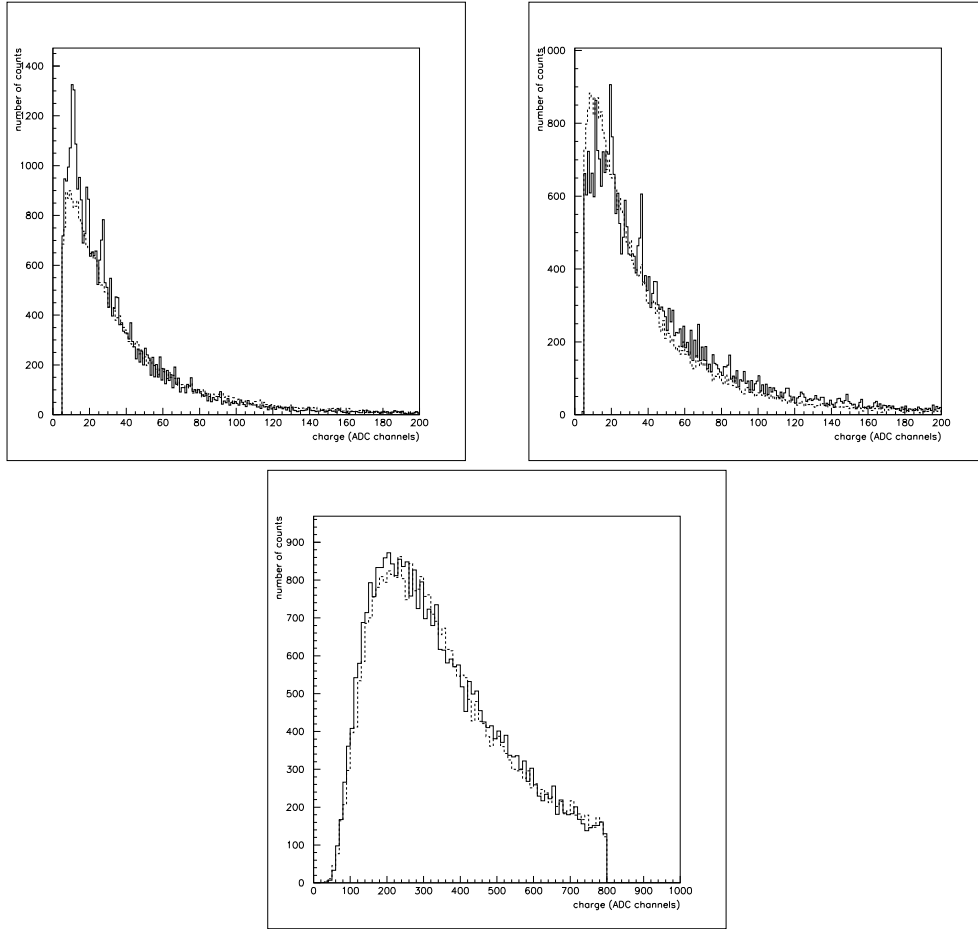
16

Figure 3.9: Comparison between the measured charges (solid lines) and calculated charges (dashed lines) on the central and the two adjacent pads.

V anode (V)		1375	1400	1425	1450	1475	1500
PLANE 1	Unworkable evts (%)	1.5	0.7	0.7	0.4	0.3	0.3
	2 sat. adj. pads (%)	0.7	0.9	1.3	1.8	2	3.9
	1 pad (%)	2.8	1.2	0.4	0.2	0.1	0.
	2 adj. pads (%)	31.0	21.2	12.7	7	3.8	1.7
	3 adj. pads . (%)	61.0	71.4	77.7	77.6	71.0	57.6
	cent. pad sat. (%)	2.9	4.5	7.2	12.4	22.2	36.5
PLANE 2	Unworkable evts (%)	0.4	0.3	0.6	0.3	0.3	0.3
	2 sat. adj. pads (%)	0.8	1.4	2.2	3.2	5.2	8.8
	1 pad (%)	0.2	0.1	0.0	0.0	0.0	0.0
	2 adj. pads(%)	48.7	41.6	27.9	19.4	10.9	5.2
	3 adj. pads (%)	47.6	53.2	64.5	69.1	69.5	62.7
	cent. pad sat. (%)	2.2	3.3	4.8	7.9	14.0	23.1

Table 3.2: Pad configuration repartition (percentage) for each cathode plane versus the HV value.
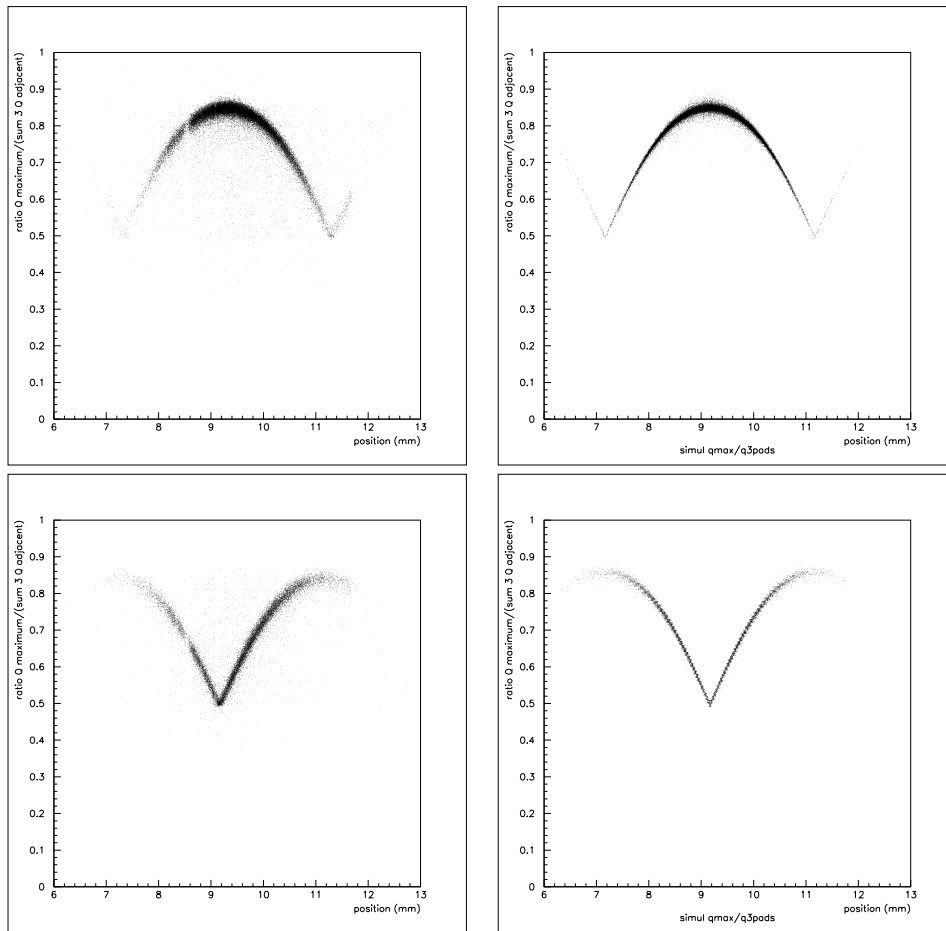
17

Figure 3.10: Comparison between experimental (left side) and simulated values (right side) of the ratio Q on the central pad divided by the sum of charges on the central and the two adjacent pads. The first plane is in the upper part of the figure.
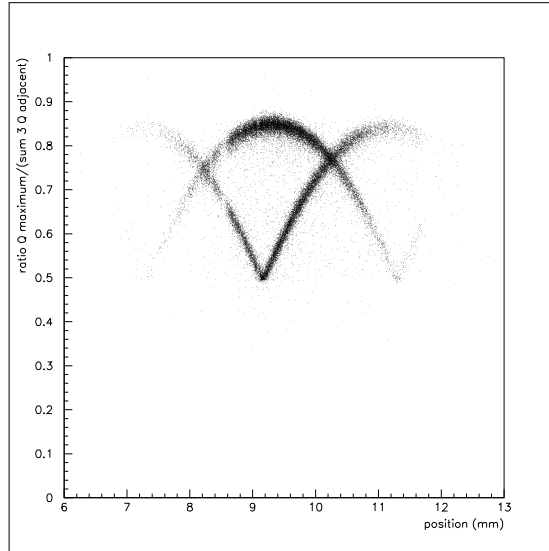
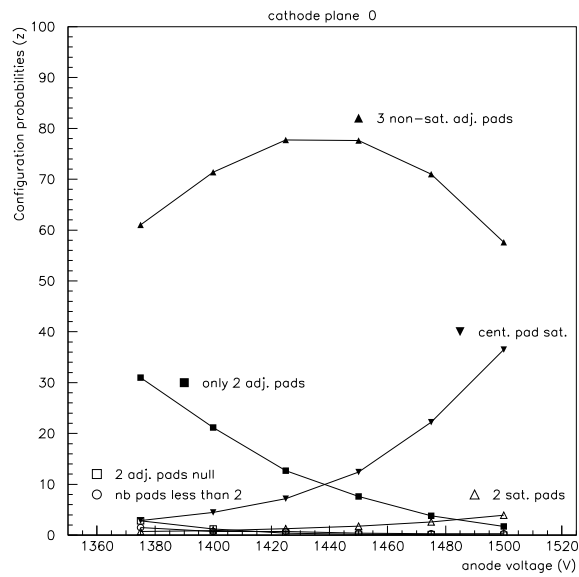Figure 3.11: Ratio R measured on both cathode planes.

Figure 3.12: Pad configuration repartition (percentage) for cathode plane 1 versus the HV value.
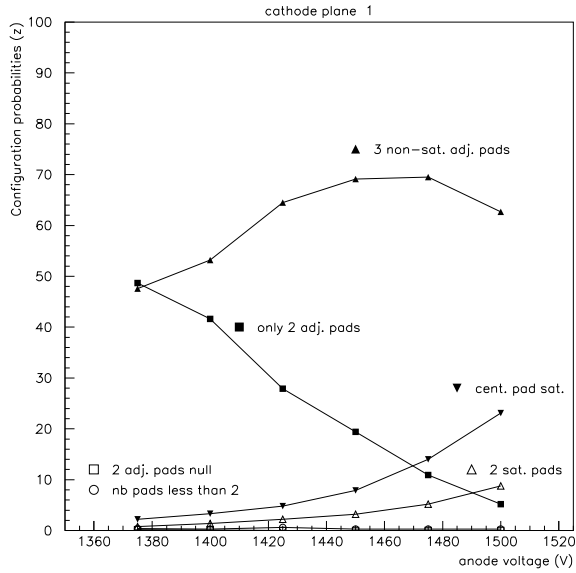
Figure 3.13: Pad configuration repartition (percentage) for cathode plane 2 versus the HV value.
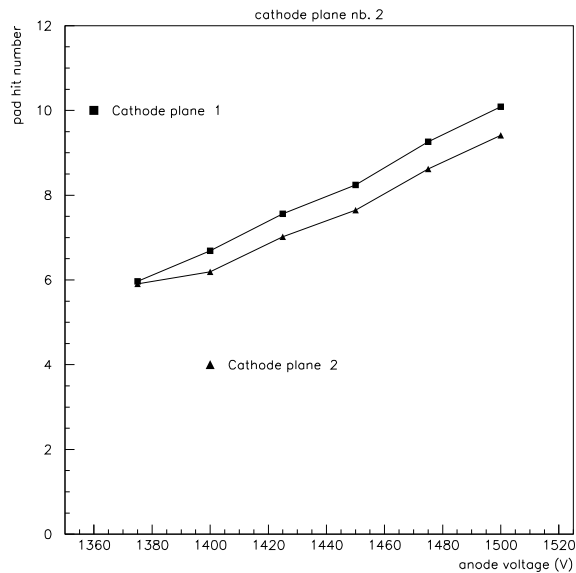

Figure 3.14: Number of hit pads for both planes versus the HV value.
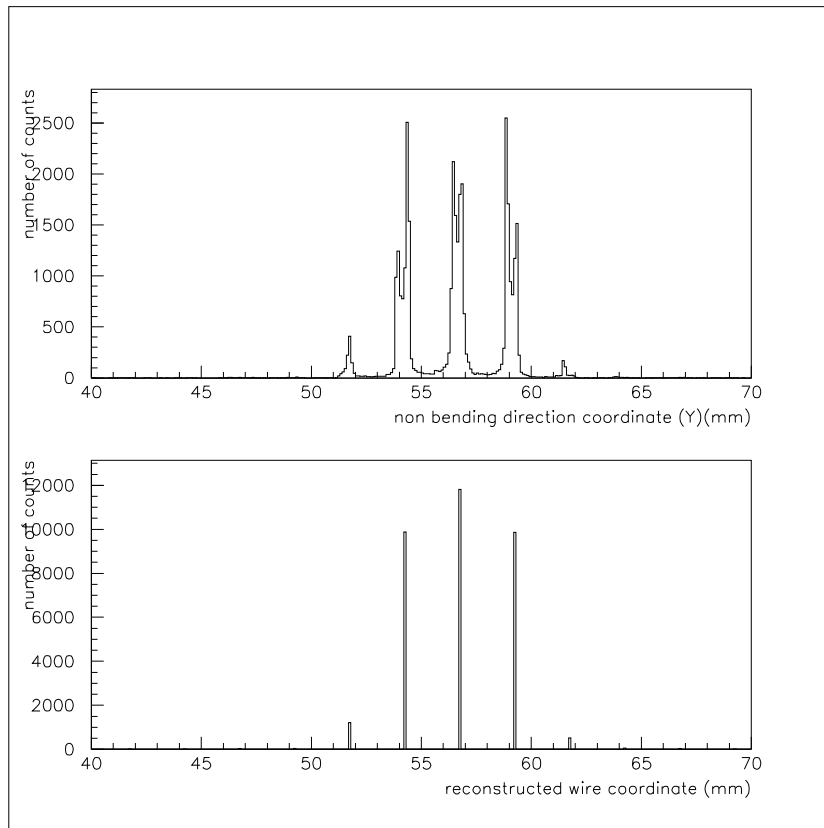
Figure 3.15: Reconstructed non-bending coordinate (Y) (mm) (upper part) and corresponding wire positions

3.4 Analysis by charge distribution fits

3.4.1 Standard procedures

A cluster of hit pads was determined around the pad corresponding to the maximum charge deposit. A two dimensional fit of X, Y positions and total charge using a Mathieson function was then performed taking center of gravity position and total measured charge as starting values. A χ^2 fitting procedure led to the best values for the three free parameters. In the non-bending direction the position of the nearest wire was then deduced from the Y value. The measured hit distribution in the non-bending direction and the reconstructed wire coordinates are shown in fig. 3.15 for HV=1450 V. The usual double peak (around 500 μm inter-distance) is observed for each wire: this effect is usually attributed to a non symmetrical avalanche around the wire.

For the bending direction, a typical spectrum of resolution as a function of the hit position is shown in fig. 3.18. A resolution of 49 μm was obtained for configuration 1 by selecting hits on one single wire (left part of fig. 3.19). It can be noticed that an adjustment with K_3 and d as free parameters leads to the values previously determined in 3.2.2. The simulation (right part of fig.
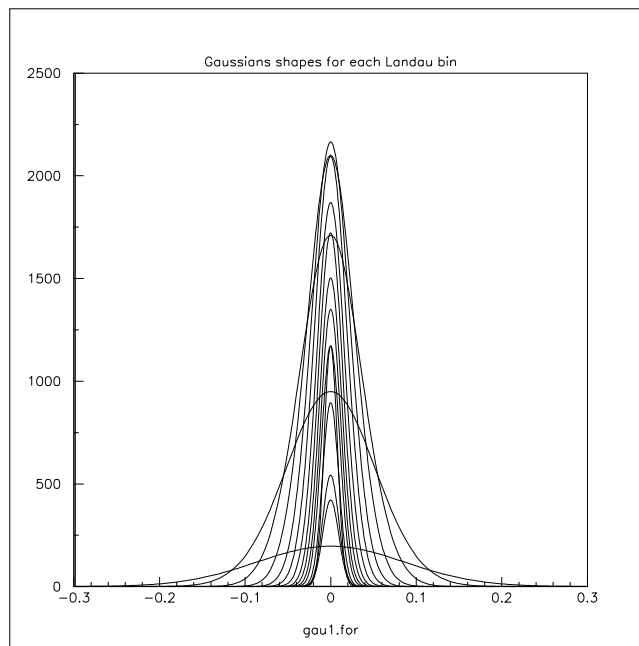
Figure 3.16: Every gaussian curve represents the spatial resolution obtained for a given energy loss bin in the chamber.

3.19) gives a resolution of 23 μm which is approximately two times better than the experimental value. This feature has not yet been explained. The tail outside of the gaussian fits are due to the dynamics of the pulse height (see Landau distribution fig. 3.2 or 3.3). To demonstrate this behaviour, the Landau distribution has been divided in x slices, and, for each charge bin, the spatial resolution has been fitted by a gaussian distribution. Higher is the measured charge, better is the obtained resolution leading to very different gaussian curves (as shown in fig. 3.16). The sum of several gaussian distributions being not gaussian explains the presence of a tail in the global resolution (see fig. 3.17)

3.4.2   Analysis for different charge configurations

Similar procedure was adapted for configurations 2 and 4. In the case of configuration 2 (saturated central pad), only the lateral pad charges are used for the fit. In the case of configuration 4 (only two pads hit), a one dimensional fit is performed in the bending direction.

The results for each cathode plane as a function of the high voltage values for the different pad configurations are shown in fig. 3.20 and fig. 3.21

The reconstruction efficiency is defined by the number of tracks which lies within $\pm 3\sigma$ (± 300 μm for respecting the detection requirements) from the true position as given by the silicon tracker.   The values for the reconstruction efficiencies as a function of HV are given in table 3.3

Then, general efficiencies, defined as the ratio of the total number of reconstructed events for all configurations (in the ± 300 microns window previously defined) to the total number of events, are reported in table 3.4 as function of the high voltage. It was previously noticed that the number of configurations of events with two saturated pads increases with high voltage. As it is not possible to analyse them, this effect make the efficiency value begin to decrease around
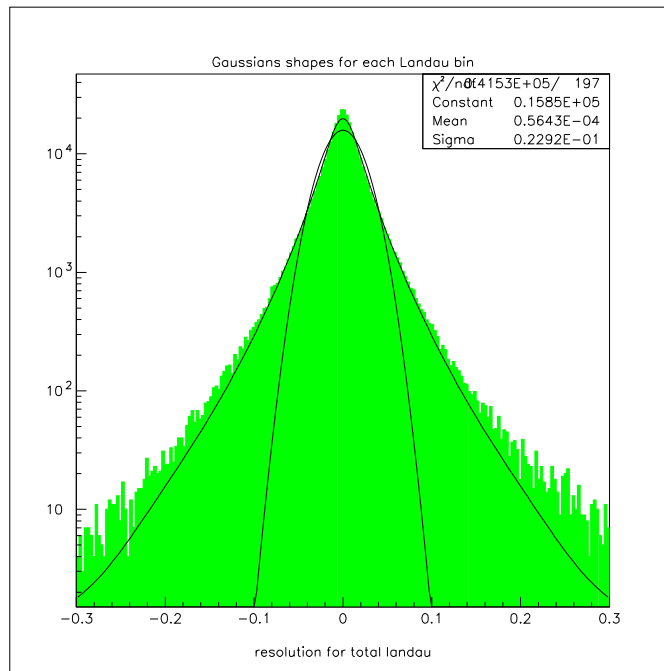
Figure 3.17: Overall spatial resolution obtained for all the energy losses in the chamber.
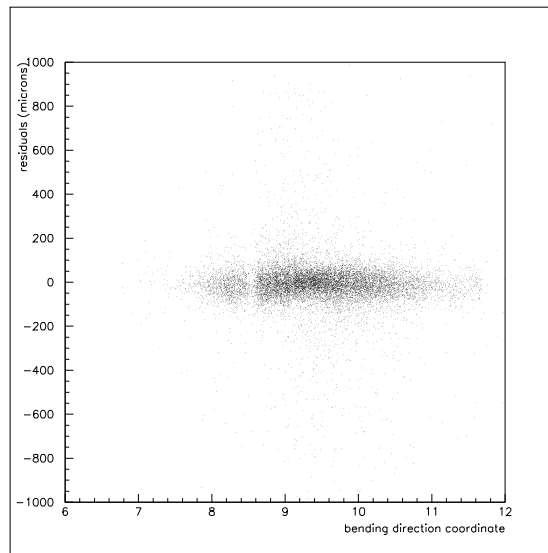

Figure 3.18: Residuals (μm) versus the coordinate (mm) along the bending direction.
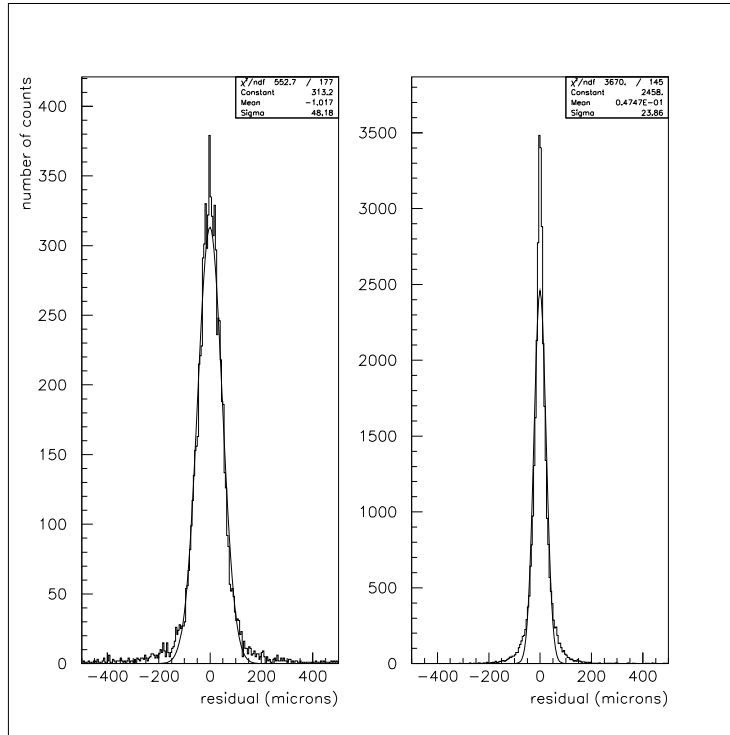
23

Figure 3.19: Experimental resolution (left part) and simulated resolution (right part) (μm) (Mathieson fit procedure).
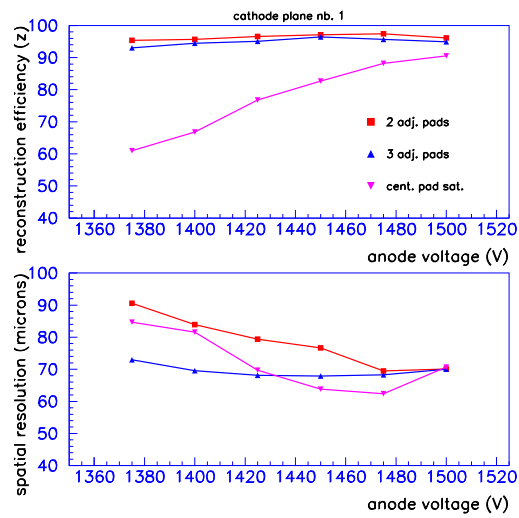

Figure 3.20: Reconstruction efficiency and spatial resolution of the first cathode plane for different pad configurations versus the HV values (Mathieson fit procedure).
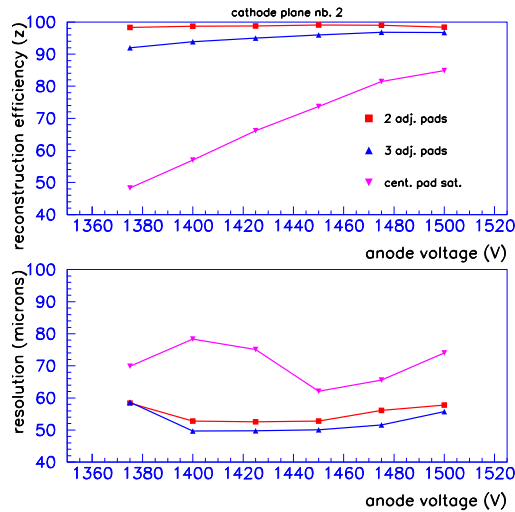
Figure 3.21: Reconstruction efficiency and spatial resolution of the second cathode plane for different pad configurations versus the HV values.

1475V for the first cathod plane and for 1400 V in the case of the second cathod plane. In order to foresee what will be the efficiency for the definitive prototype (and its electronics constructed to have a larger dynamics range and no saturation effects) we calculate the efficiency assuming that events with saturated pads (two and one respectively in table 3.4) will be analysed as 3 pads configurations. Efficiencies values reach 95% (96 %) in the case of the first (second) cathod plane with a plateau of 50V (at least) around 1475V.

One of the advantage of two staggered pad planes is to increase the chamber efficiency by using the difference of impact point relative to the pads. Thus in order to evaluate the total efficiency of the chamber, the second plane has also been taken into account when the first one was inefficient. The results for both planes are displayed in fig. 3.22 and fig. 3.23. For example at 1450V, around 92% of the 4.7% inefficiency of the plane 1 is calculated, so that, an overall efficiency of 99.6% should be reached by using the two planes information.

The difference of spatial resolution between the two planes is due to the relative location of the impact point relative to the pads. This effect is illustrated in fig. 3.24 where the spatial resolutions are shown in bins of 0.25 mm for both the planes.

3.5 Analysis by center of gravity method

In the second method, a calculation of the center of gravity of the three measured charges has been performed. To take into account the non-linearity of the charge repartition, a numerical correction has to be invoked for achieving the best possible resolution. This is achieved by fitting the residual as function of the true hit position (given by the silicon tracker) with a 6th order polynomial. The

V anode	Pad configuration		1375	1400	1425	1450	1475	1500
PLAN 1	2 adjacent pads	eff. (%)	95.4	95.7	96.6	97.1	97.4	96.1
		res. (μm)	90.6	83.9	79.4	76.7	69.5	70.1
	3 adjacent pads	eff. (%)	93.0	94.5	95.1	96.4	95.7	94.9
		res. (μm)	73.	69.6	68.1	67.9	68.3	70.
	central pad saturated	eff. (%)	61.0	66.8	76.8	82.7	88.2	90.5
		res. (μm)	84.7	81.6	69.7	63.8	62.4	70.7
PLAN 2	2 adjacent pads	eff. (%)	98.3	98.7	98.8	99.1	99.0	98.4
		res. (μm)	58.4	52.8	52.6	52.8	56.1	57.8
	3 adjacent pads	eff. (%)	92.0	93.9	95.0	96.0	96.8	96.7
		res. (μm)	58.7	49.7	49.8	50.1	51.6	55.7
	central pad saturated	eff. (%)	48.3	57.0	66.1	73.7	81.5	84.9
		res. (μm)	69.9	78.3	75.1	62.1	65.6	74.

Table 3.3: Reconstruction efficiencies and spatial resolutions of the two planes versus the HV values for different pad configuration types.

V anode (V)		1375	1400	1425	1450	1475	1500
PLANE 1	Global efficiencies (%)	88.1	90.8	91.7	91.9	91.2	89.3
	Global eff. (%) corrected for two saturated pad events	88.5	91.4	92.7	93.4	93.0	92.8
	Global eff. (%) corrected for all saturations	89.7	92.9	94.2	95.3	94.8	94.6
PLANE 2	Global efficiencies (%)	92.7	92.9	92.0	91.4	89.5	85.3
	Global eff. (%) corrected for two saturated pad events	93.1	93.7	93.5	93.8	93.7	92.8
	Global. (%) corrected for all saturations	94.2	95.4	95.5	96.2	96.4	96.6

Table 3.4: Global efficiencies as function of high voltage. See explanations of corrections in the text
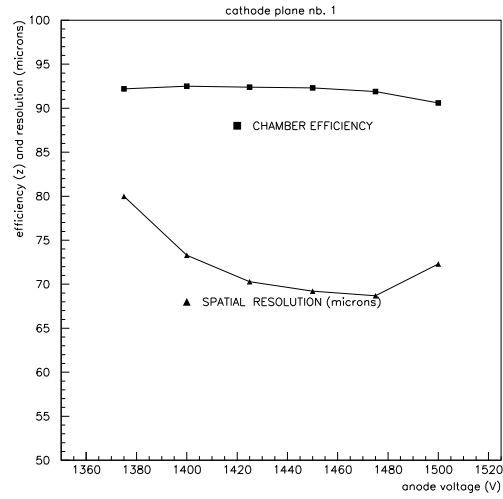
Figure 3.22: Global efficiency and spatial resolution of the chamber obtained by using the plane 2 in case of inefficiency of the first one.
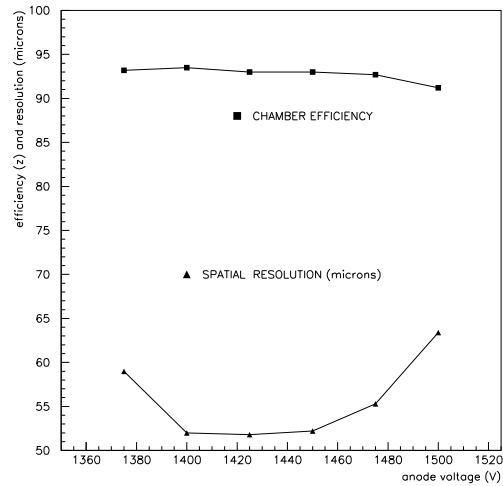

Figure 3.23: Global efficiency and spatial resolution of the chamber by using the plane1 in case of inefficiency of the second one.
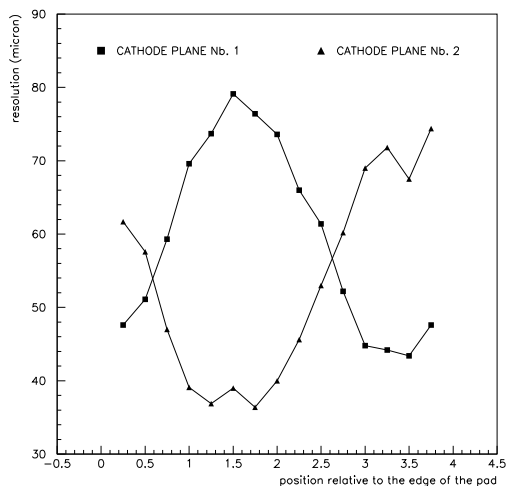
Figure 3.24: Spatial resolution in both planes versus the impact location relative to the edge of one pad of the first cathode plane (Mathieson fit procedure).

HV value (V)	1375	1400	1425	1450	1475	1500
Resolution (μm)	56.6	51.5	51.2	51.4	53.5	57.3
Efficiency (%)	97.5	98.1	98.2	98.2	98.1	97.3

Table 3.5: Reconstruction efficiency and spatial resolution obtained by the c.o. g. method applied for the first cathode plane.

different steps of the correction for both planes are presented in fig . 3.25.

The results are given in table 3.5 for the first plane and in table 3.6 for the second plane. It is to be noted that:

- the results have been obtained only for the charge configurations with three pads hit with no saturation.

- the reconstruction efficiency is defined as being the ratio of the integral of the counts in a window of ± 300 μm (corresponding to $\pm 3\sigma$ of the requirements) over the total number of counts in the spectra.

HV value (V)	1375	1400	1425	1450	1475	1500
Resolution (μm)	55.8	51.7	53.2	56.0	58.4	64.5
Efficiency (%)	96,5	97.0	97.3	97.6	97.3	96.5

Table 3.6: Reconstruction efficiency and spatial resolution obtained by the c.o. g. method applied for the second cathode plane.
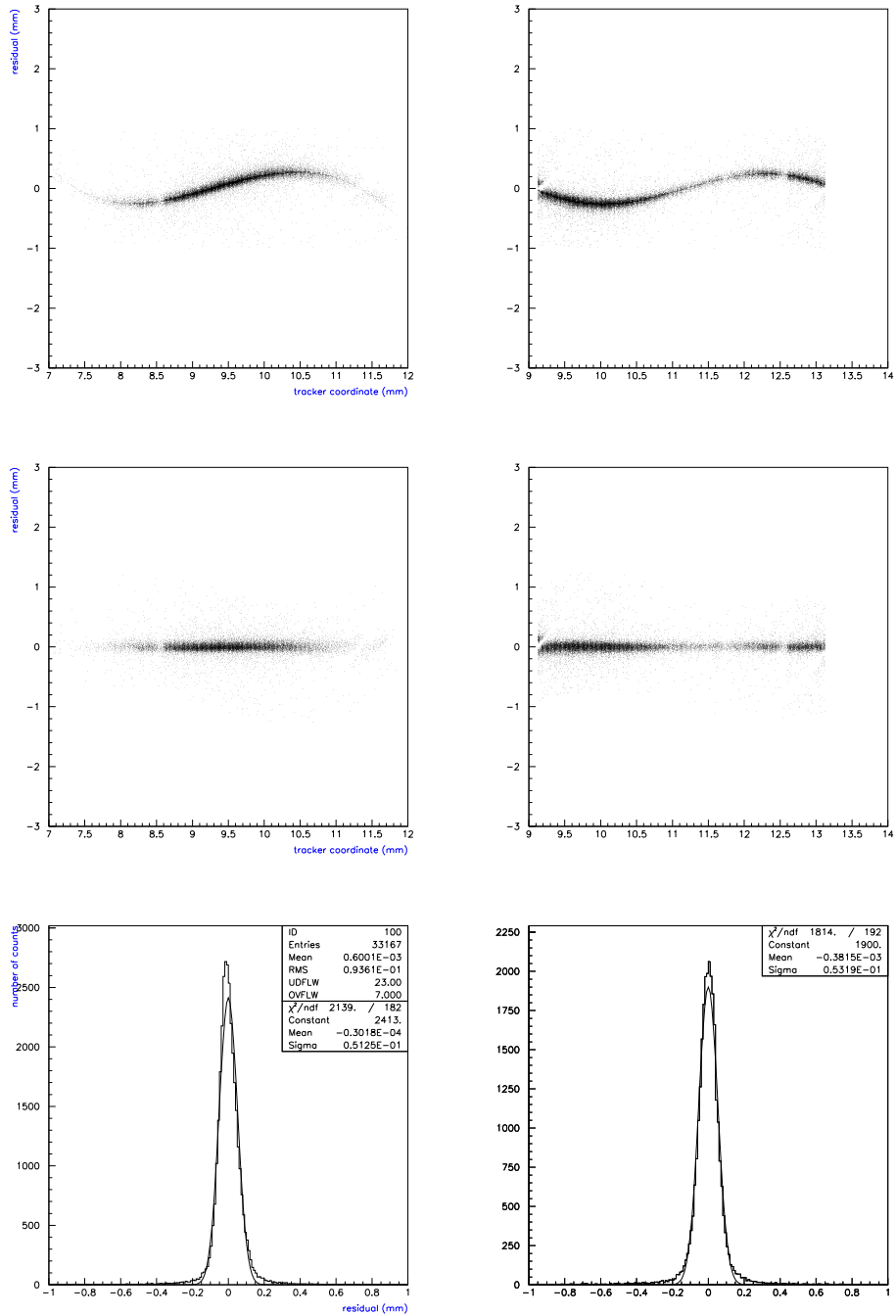
Figure 3.25: Residuals measured on plane 1 (left column) and plane 2 (right) versus the position given by the silicon tracker. Aberrations with the polynomial fits are in the upper part, the corrected measured positions are in the middle and the residuals are in the lower part.
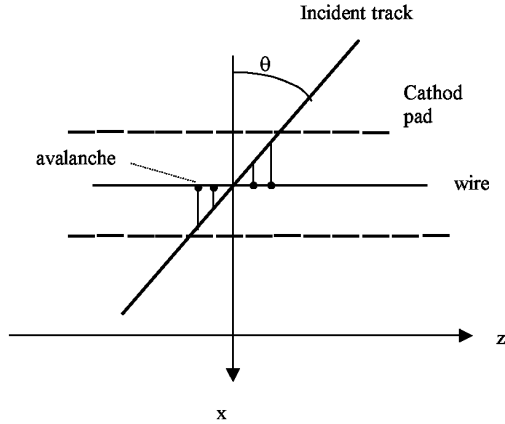
Figure 3.26: Definition of the incident angle.

3.6 Incident angle influence

3.6.1 Experimental results:

It has already been shown [3] that the spatial resolution was weakly dependent on the trajectory angle in the direction perpendicular to the wires. We only performed the measurements for different incident trajectory angles along the wires as shown in fig. 3.26. The chamber was inclined up to 38^0 and the analysis has been done based on the Mathieson fit procedure with the parameters which were optimized for orthogonal tracks. The c.o.g. method has also been applied . Results are shown in fig. 3.27 which have been obtained for events corresponding to the configuration 1 of paragraph 3.3 (i.e. 3 adjacent pads, without saturation in the bending plane) at HV= 1425 V.

The fluctuations in the amount of ionisation occurring in discrete positions along the trajectory will affect the charge distribution symmetry along the anode wire. The resulting effect is an additional error in the charge centroid measurement which can be parameterized as:

$\sigma_\theta = b \frac{sin\theta}{\sqrt{cos\theta}}$

The solid curve in fig. 3.27 is a fit of the classical phenomenological form [7]:

$\sigma = \sqrt{\sigma_0^2 + b^2 \frac{sin^2\theta}{cos\theta}}$

The best values are σ_0 =53 μm and b= 554 μm

The resolution versus θ angle has also been studied for several classical reconstruction algorithms [6] and the results are shown in figures 3.27 and 3.28. The spacial resolution was found to degrade rapidly with the angle and the behaviour was same for all the four methods. The average fraction of the charge deposited on the central pad decreases from around 80% at 0^0 down to 72% at 38^0 .
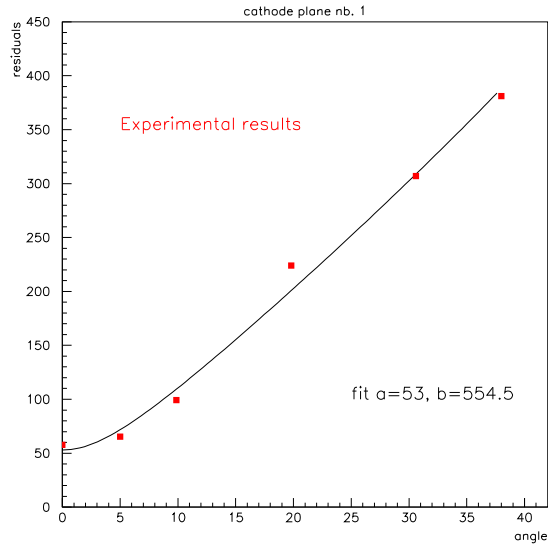
Figure 3.27: Spatial resolution versus the incident angle along the wires obtained with the Mathieson method.
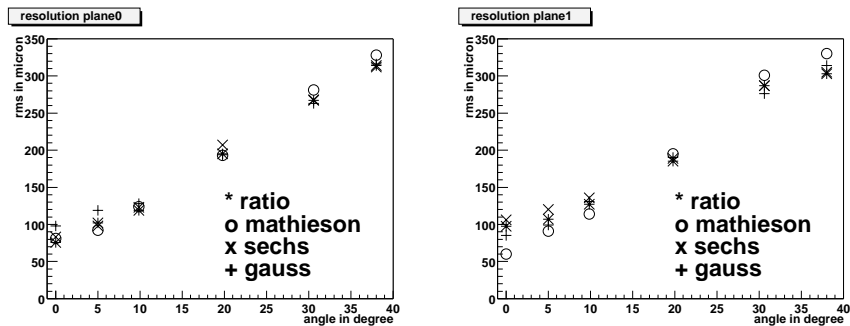

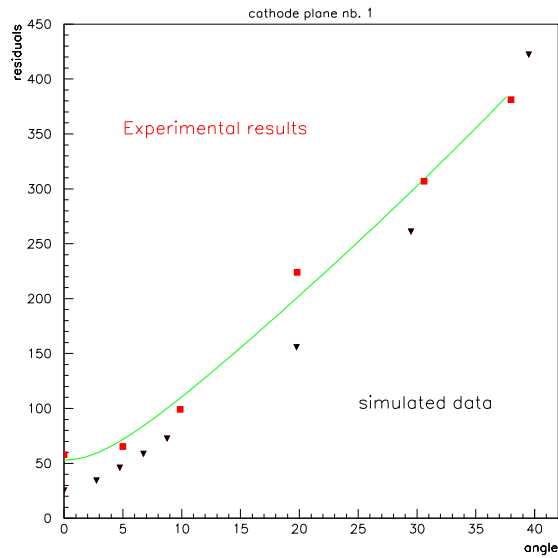Figure 3.28: Resolution as a function of angle of the track for the four algorithms.

31

Figure 3.29: Comparison between experimental and simulated resolutions together with the fitted curve versus the incident angle.

3.6.2 Simulations:

A Monte-Carlo code developed by V. Cherniatine and A. Chikanian was used, taking into account the following physics processes along the track:

1. creation of primary clusters in the gas

2. diffusion of the electrons as they drift to the anode wire according to their range

3. multiplication of electrons on the anode wire according to the gain of the chamber

4. induced charge on cathode

5. addition of electronic noise

As the different parameters (gain, gas mixture) were not completely adapted to our prototype, only the variation of the resolution versus the angle was relevant which has been shown in fig. 3.29.

Chapter 4

Conclusion

In beam tests of a small prototype with the chosen geometry for cathode pads and anode-cathode gap for Station 1, have been performed. The analysis have showed that the requirement of 100 μm resolution in the bending plane is fulfilled : a mean value of 67 μm (54 μm) for the first (second) cathod plane and all configurations, has been extracted at 1475 V. The efficiency is around 95% in a ±300 μm resolution window for one cathode plane and in a dynamics range of ±25V around 1475V.The deterioration of spatial resolution as a function of the incident angle was found to be within reasonable limits for the physical trajectories of the Dimuon Arm (θ<9^0). Simulations have been performed to reproduce the experimental data. The experimental resolution is worse than the simulated resolution by a factor ~ 2. This is not yet explained and "ad hoc" calibration factors were introduced in the simulation in order to explain this discrepancy. The worst simulation obtained through simulation was around 30 μm. The tails of the distribution, on the contrary, could be well explained by the dynamics of the total charge deposit on the cathode (Landau distribution).

Bibliography

[1] ALICE Technical Design Report- Dimuon Forward Spectrometer- CERN/LHCC, 99-22 (1999) and Addendum.

[2] ALICE DATE, User's guide, Internal Report ALICE 98/44 (1998).

[3] L. Kharmandarian Thesis (1999) Internal Report IPNO-T 00-02.

[4] E. Mathieson and J.S. Gordon, Nucl. Instr. and Meth., A234 (1984)277.

[5] J.C.Santiard et al., communication to "6thPisa meeting on advanced detectors", la Biadola, Isola d'Elba, Italy- Internal Report CERN-ECP, 94-17 (1994) and J.C. Santiard, Internal note n^{0}2, EP/MIC, 01-09-95 (1995).

[6] R. Wurzinger, Y. Le Bornec and N. Willis, Internal report Institut de Physique Nucleaire Orsay, IPNO-DRE 96-08(1996).

[7] K. Lau et al, Nucl. Inst. and Meth. in Phys. Res. A354(1996)376.

Contents